Nuclear Engineering and Design 458 (2026) 115115

Contents lists available at ScienceDirect

Nuclear Engineering and Design

journal homepage: www.elsevier.com/locate/nucengdes

Design and commissioning of new facility CORELLA-2 for erosion-corrosion tests in liquid Pb and LBE at high temperature

Renate Fetzer *, Louis Müller, Fabian Lang, Annette Heinzel, Alfons Weisenburger, Georg Müller

Institute for Pulsed Power and Microwave Technology (IHM), Karlsruhe Institute of Technology (KIT), Hermann-von-Helmholtz-Platz 1, 76344 Eggenstein-Leopoldshafen, Germany

ARTICLE INFO

Keywords:
Erosion-corrosion
Heavy liquid metal
Liquid Pb
Flowing condition
Oxygen control
Test facility

ABSTRACT

Liquid lead (Pb) and lead-bismuth eutectic (LBE) are attractive heat-transfer fluids for energy-related technologies despite their chemical aggressiveness towards solid materials. In this work, the new erosion-corrosion test facility CORELLA-2 is introduced and its design and commissioning are reported. CORELLA-2 is a rotating machine that enables corrosion studies of up to six specimens of arbitrary shape in liquid Pb and LBE under flowing conditions. The facility is designed for temperatures up to 700 °C and allows controlled adjustment of the dissolved oxygen content thanks to the use of corrosion- and oxidation-resistant components. Numerical simulations of the flow field supported the design of the facility and provide information on the relative speed between the specimens and the liquid metal. First experiments performed in liquid Pb at a relative speed of 1 m/s and a temperature of 450 °C demonstrate successful commissioning of the new erosion-corrosion test facility CORELLA-2.

1. Introduction

Heavy liquid metals such as lead (Pb) or lead-bismuth eutectic (LBE) are promising heat transfer fluids in energy-related technologies due to their excellent thermal properties. Examples are Gen-IV fast reactors, accelerator-driven systems, concentrating solar power, or thermal energy storage systems (Alemberti, 2016; Wallenius, 2019; Heinzel et al., 2017; Vignarooban et al., 2015; Pantaleo et al., 2024; Niedermeier, 2023). One of the main challenges when using Pb or Pb alloys as heat transfer fluid is their chemical aggressiveness towards structural materials, in particular when exposed to extreme conditions. The latter include regions experiencing very high temperature or high flow rates of the heat transfer fluid.

Due to the high solubility of steel constituents like Ni and Cr in liquid Pb or LBE at elevated temperatures, steel surfaces in contact with the liquid metal may be heavily corroded by dissolution combined with heavy liquid metal penetration. Structural and phase changes (ferritization), degradation of the mechanical properties, and finally material failure may result (Zhang, 2009; *Handbook on Lead-bismuth Eutectic Alloy and Lead Properties, Materials Compatibility, Thermal-hydraulics and Technologies*, 2015). By adding an appropriate amount of oxygen to the liquid Pb or LBE, an oxide layer can grow on the steel surfaces and protect the material from dissolution attack. However, high oxygen concentrations can lead to excessive growth of thick oxide scales, which impede heat transfer and bear the risk of spallation. At temperatures below 550 °C and with a concentration of 10^{-6} wt% oxygen dissolved in the liquid metal, austenitic steels typically form oxide layers with a duplex or single layer structure, depending on the surface and operation conditions. The duplex-layer oxides consist of an outward-growing layer of magnetite and an inward-growing Fe—Cr spinel layer (*Handbook on Lead-bismuth Eutectic Alloy and Lead Properties, Materials Compatibility, Thermal-hydraulics and Technologies*, 2015). The dense and stable spinel layer forms both in stagnant and flowing conditions, whereas the porous and mechanically less stable magnetite might not be observed in flowing conditions (Weisenburger et al., 2008). At lower oxygen concentration (~10^{-7} wt%), the oxidation kinetics is slowed down and mainly Cr is oxidized. The thin Cr-oxide layer is protective only at temperatures up to about 400 °C (Tsisar et al., 2014; Tsisar et al., 2016). In oxygen-poor conditions (~10^{-8} wt% and below), the dominant corrosion mechanism is dissolution (Lambrinou et al., 2017).

With increasing temperature, both the oxidation kinetics and dissolution are enhanced. Fe- and Cr-based oxide scales are not protective

* Corresponding author.
E-mail address: renate.fetzer@kit.edu (R. Fetzer).

https://doi.org/10.1016/j.nucengdes.2026.115115
Received 7 May 2026; Received in revised form 26 June 2026; Accepted 14 July 2026
Available online 20 July 2026

anymore and dissolution corrosion of common steels occurs (Wang et al., 2022; Wang et al., 2024; Purwitasari et al., 2025a; Purwitasari et al., 2025b). The situation may substantially improve when *Al*-containing alloys are used, which enable selective oxidation of *Al* and the growth of an *Al*-rich oxide scale. Compared with Fe- or Cr-based oxides, Al oxide grows more slowly and forms a denser and more stable oxide scale, which substantially improves the corrosion resistance at high temperature or low oxygen concentration (Takaya et al., 2012; Popovic et al., 2018; Shi et al., 2019; Dömstedt et al., 2020; Shi et al., 2021; Dömstedt et al., 2019; Cionea et al., 2016; Popovic et al., 2019).

In most applications of liquid metal technology, the liquid metals are in motion. In addition to the chemical interaction between the liquid Pb/LBE and the solid material that leads to its corrosion as described above, fluid flow additionally adds to the material degradation. Depending on the flow conditions, various types of erosion-corrosion may be distinguished. Flow-accelerated corrosion denotes chemical corrosion (i.e., dissolution as in stagnant conditions), where the liquid flow enhances the transport of dissolved material from the solid surface to the liquid bulk and thus accelerates the dissolution process. Hereby, the mass transport depends on the local flow conditions such as the wall shear stress or the near-wall turbulence level (Wan and Saito, 2018). At high speeds, the liquid flow additionally imposes significant mechanical stress on the solid surfaces, which may result in mechanical erosion. This becomes even more severe when solid particles are dispersed in the flowing liquid and impinge on the solid surfaces, leading to abrasion. Erosion is very actively researched in aqueous and oil solutions (pipelines, etc.), whereas literature on erosion-corrosion in heavy liquid metals is rather scarce.

To generate flow of liquid Pb/LBE, either forced convection loops or rotating machines might be used. Forced convection loops use pumps to drive the flow of the liquid metal and typically operate at non-isothermal conditions. In non-isothermal systems, the temperature-dependent solubility results in a continuous mass transport of dissolved material from hot regions with on-going dissolution to colder regions, where the dissolved material re-precipitates. Available forced convection loops operate at flow speeds up to about 2–3 m/s in the test section in accordance with the envisaged flow in the core of lead-cooled fast reactors (Wan and Saito, 2018; Fazio et al., 2003; Schroer et al., 2011). However, much higher relative velocities between the liquid metal and solid components with values up to 10 m/s are expected for pump impellers. Such high speeds might be achieved by rotating machines.

Rotating machines are operated at isothermal conditions. The flow of the liquid metal is driven by rotating components (inner cylinder or disk) inside a stationary container. The test specimens are either held at a fixed position within the generated flow field or mounted on the rotating component. Numerous designs of rotating machines are published (Kondo et al., 2011; Chakraborty et al., 2015; Jiang et al., 2020; Choi et al., 2021; Li et al., 2021a; Li et al., 2021b; Chen et al., 2020; Martinelli et al., 2020; Ali et al., 2022; Wong et al., 2024; Wong et al., 2026), some of them solely based on detailed CFD simulations of the flow field (Ali et al., 2022; Wong et al., 2024). However, ready-made facilities available for erosion-corrosion testing in liquid Pb/LBE are less numerous (Choi et al., 2021; Li et al., 2021a; Li et al., 2021b; Chen et al., 2020; Martinelli et al., 2020; Wong et al., 2026). The rotating disk facility in Korea holds the samples snug fitted into the rotating disk (published experiment: LBE with $\sim 3 \times 10^{-8}$ wt% oxygen, velocity range $\sim$ 0.5–3 m/s, 600 °C, 150 h), which does not allow variations in the sample geometry and orientation (Choi et al., 2021). In the rotating cylinder machine in China, the samples are directly mounted on the rotating cylinder (Li et al., 2021a; Li et al., 2021b). Corrosion on both the sample surfaces oriented parallel to the flow and the ones perpendicular to the flow was studied in oxygen-saturated LBE (test conditions: 1 and 5 m/s, 400 °C, 1000 h). Similarly, the rotating disk facility built in China (3 m/s, 550 °C, 1500 h) operates in LBE at oxygen-saturated conditions due to the absence of an oxygen control system (Chen et al., 2020). In the CICLAD facility (France) the cylindrical samples are fixed to the rotating shaft (angular velocity from 35 to 450 rad/s) (Martinelli et al., 2020). The rotating machine CICLAD is combined with a loop for removal of dissolved corrosion products from the liquid metal. Published data were obtained at very low oxygen contents of the LBE (10^{-8} wt% for 1-day exposures, even less for longer exposure tests up to 790 h). The ECO-Rig in Sweden (Wong et al., 2026) allows the investigation of four cylindrical specimens at the same time, fixed on a rotating disk at an angle of 30 degrees from the radial direction to maximize the shear rate at given speed. The published experiment ran for 288 h in Pb at 500 °C with $\sim 10^{-8}$ wt% O and a sample speed of up to 9.9 m/s. The liquid metal flow was not considered.

The published exposure tests in Pb/LBE-filled rotating machines operated either at oxygen-saturated conditions (Li et al., 2021a; Li et al., 2021b; Chen et al., 2020) or at very low dissolved oxygen concentrations ($\sim 10^{-8}$ wt%) not sufficient to form protective oxide scales on the surfaces of the test samples (Choi et al., 2021; Martinelli et al., 2020; Wong et al., 2026). The latter also turned out to be an issue of the previous CORELLA facility due to excessive oxidation of the chamber interior during the exposure tests (Heinzel et al., 2024). The CORELLA facility at Karlsruhe Institute of Technology (KIT) was a fully operational erosion-corrosion test facility with a rotating inner cylinder (Heinzel et al., 2024; Kieser et al., 2009; Fetzer et al., 2021). The specimens were mounted at a fixed position within the flow field generated by the rotating cylinder. Because of the free liquid surface deformation and splashing, the rotational speed of the inner cylinder was experimentally limited to 1200 rpm (rounds per minute). At this speed, the liquid metal reached a bulk velocity of 1.6 m/s when the facility was loaded with 5 specimens (Heinzel et al., 2024; Fetzer et al., 2021). Responsible for the rather low flow velocity were the turbulent nature of the flow and the decelerating effect of the fixed specimens. Both effects were not taken into account in the design stage of the facility, which resulted in an originally predicted flow velocity of up to 20 m/s (Kieser et al., 2009).

In order to achieve higher relative velocities between the specimens and the liquid metal (Pb or LBE) and to enable oxygen contents between depleted and saturated conditions, a new rotating machine called CORELLA-2 has been designed and built at KIT. The facility has been successfully commissioned and first results of the commissioning test are available. This study presents the design of CORELLA-2, numerical simulations of the flow field generated during its operation, and the first operation test demonstrating the functioning of the new erosion-corrosion test facility.

2. Design of CORELLA-2

The main design goals of the new erosion-corrosion test facility CORELLA-2 are (i) to achieve a high relative velocity of at least 4 m/s between the specimens and the liquid metal (Pb or LBE), (ii) to enable erosion-corrosion tests of specimens with different geometry (cylindrical and flat) and orientation, (iii) to ensure a reliable setting of the oxygen content in the liquid metal, and (iv) to enable operation at test temperatures up to 700 °C.

2.1. Oxygen control system

Oxygen control in CORELLA-2 is achieved via the gas phase above the liquid pool as in the previous facility CORELLA. A continuous flow of an Ar/Ar-5%H_2 gas mixture with defined H_2/H_2O ratio (achieved by streaming the gas through water at a specific temperature) is used to fix the oxygen partial pressure in the gas phase above the liquid metal and to supply or remove oxygen to/from the system. Oxygen is either supplied to or removed from the liquid metal via transfer across the liquid-gas interface until thermodynamic equilibrium is achieved between the concentration of oxygen dissolved in the liquid metal and the set oxygen partial pressure in the gas phase. Since this process takes several hours to days depending on the initial conditions, amount of Pb/LBE, and

transport properties inside the liquid metal (extent of convection), the liquid Pb/LBE is preconditioned to the desired oxygen content and temperature in a conditioning chamber before it enters the test chamber with the specimens, see Fig. 1a for the design and Fig. 2 for a photograph of the final facility. In addition to a gas inlet and outlet, the gastight conditioning chamber is equipped with sensors for the temperature, the oxygen concentration in the liquid metal, and the filling level.

Once preconditioned, the liquid Pb/LBE is transferred via a connecting pipe to the test chamber, which is also equipped with temperature, oxygen, and level sensors and an oxygen control system via the gas phase (gastight chamber, gas in- and outlet). Continuous and controlled oxygen supply via the gas phase is provided throughout the entire erosion-corrosion test to guarantee that oxygen consumption in the chamber does not lower the oxygen content of the liquid metal.

Experience from the previous CORELLA facility showed that a stable oxygen level of, e.g., 10^{-6} wt% in the liquid metal is not possible without additional corrosion protection of the chamber interior. The reason is that oxygen is consumed not only by oxide scale growth on the specimens' surfaces but also by oxidation of the interior chamber components and of dissolved species in the liquid metal. To minimize both liquid metal corrosion and oxidation of chamber components (made of stainless steel 316Ti), the main parts in direct contact with the liquid metal or its vapor phase have been aluminized prior to assembly. This applies to both the conditioning chamber and the test chamber of CORELLA-2.

2.2. Test chamber interior

In addition to the better oxygen control achieved by using chamber components with higher corrosion/oxidation resistance, the main purpose of the new facility compared with the old one is to achieve a higher relative velocity between the liquid metal and the specimens. Hereby, the facility should allow the test of both cylindrical and flat specimens, the latter with flexibility in their orientation relative to the flow. To achieve this goal, a new concept is introduced: The specimens are rotating, while the Pb/LBE is kept as stagnant as possible. The latter is achieved by forming a narrow channel for the moving specimens and by slowing down the flow in the open space above the rotating parts by four stationary plates (baffles). These baffles are L-shaped and welded to the cover plate of the chamber, see Fig. 1b. The specimens are mounted to specimen holders, which are attached to a rotating disk. This disk is not solid but contains six large holes that allow exchange and mixing of the Pb/LBE above and below the disk to enhance the oxygen transport from the surface of the liquid metal to the specimens. The oxygen sensor (Pt/air sensor with Y-stabilized Zr oxide electrolyte) is located close to the bottom of the channel to monitor the oxygen content in the vicinity of the specimens. All rotating parts (shaft, disk with sample holders, specimens) are held by a grooved ball bearing.

A schematic of the chamber interior with respective dimensions is also shown in Fig. 3. The test chamber has an inner diameter of 400 mm. The central part of the chamber's bottom plate is elevated to form a channel for the specimens. The channel is 40 mm wide and 45 mm high. The rotating parts comprise the disk (thickness 12 mm, diameter 300 mm) with the six holes (diameter 60 mm), six connectors to mount the sample holders, and up to six pairs of sample holders and specimens. Note that a symmetric loading with samples is required to avoid an imbalance of the rotating parts. Thus, either two, three, four, or six specimens and their respective sample holders are mounted to the rotating disk, with either all or at least opposing specimens having the same geometry and orientation. Up to now, specific sample holders are available for cylindrical and flat specimens, but further options are possible. The only limitation on the geometry of the specimens is the available space in the channel.

2.3. Exterior components

Both the conditioning and the test chamber are designed for operating temperatures up to 700 °C. The high temperature is achieved with heating plates below the chambers and heating wires wrapped around the walls of the chambers. Furthermore, the valves at the connecting pipe and the drain pipe can be heated. Chambers and pipes are thermally insulated, see the final facility in Fig. 2. The high temperature in the test chamber requires a cooling unit between chamber and less heat-resistant parts above the chamber. The most critical component in this respect is the rotary feedthrough for the drive shaft. It contains a magnetic fluid for the dynamic sealing and is additionally cooled by air ventilation. An electric motor is used to drive the rotation of shaft, sample holder disk, and specimens. Computerized control of rotational speed, temperature, and oxygen content (via an adjustable gas flow) are provided.

The final setup is shown in Fig. 2. The cover plates of both conditioning chamber and test chamber with all connected parts can be opened with the help of a crane.

3. Simulation of flow field

Calculation of the absolute velocity of the rotating specimens is straightforward. However, the liquid metal in the rotating machine is not at rest but moves along with the rotating parts inside the chamber. Since relevant for the effects of flow on corrosion is the relative motion

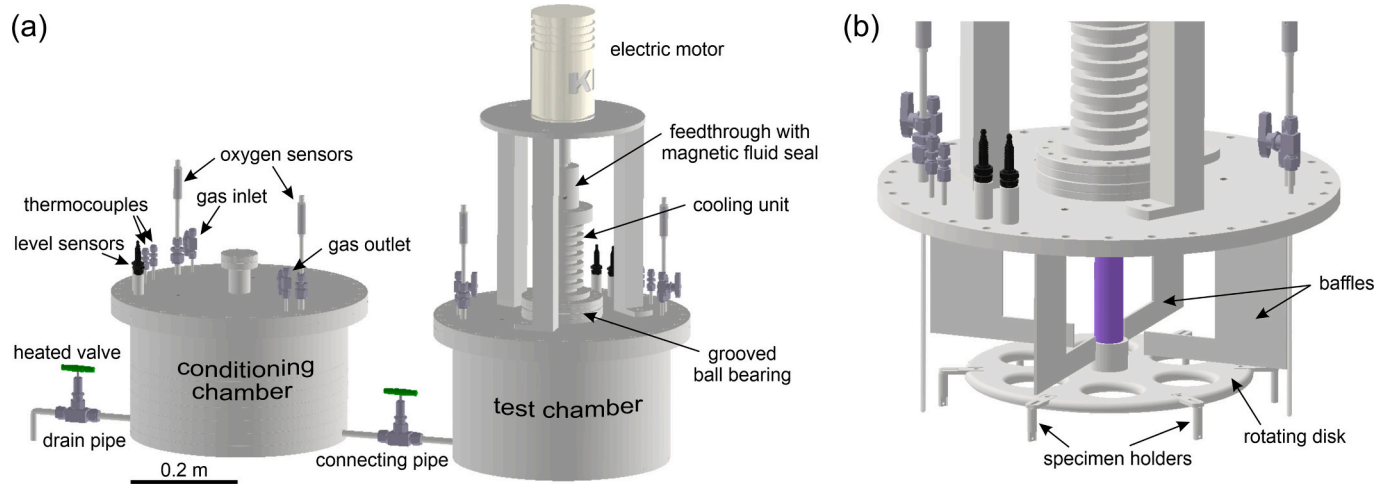

Fig. 1. Design of CORELLA-2. (a) Entire facility comprising a conditioning chamber and a test chamber, (b) interior components attached to the cover plate of the test chamber.

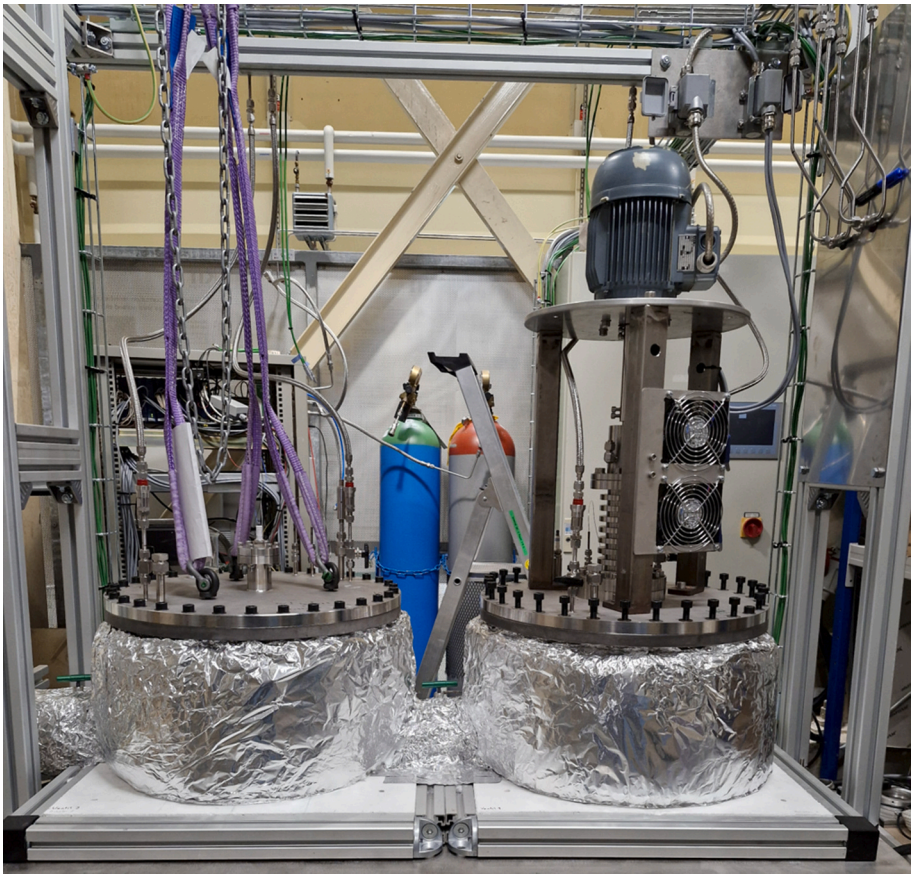

Fig. 2. Photograph of fully assembled CORELLA-2 with conditioning chamber on the left (crane ropes are attached) and test chamber on the right.

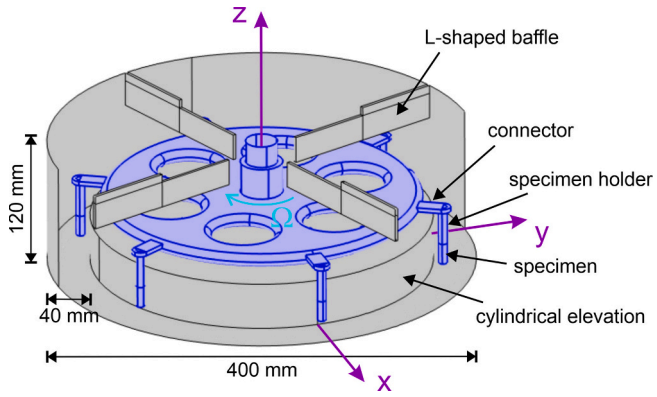

Fig. 3. Simulation domain. Blue parts rotate, grey parts are fixed in space. Some domain boundaries (free fluid surface and solid chamber wall in front) are hidden. (For interpretation of the references to color in this figure legend, the reader is referred to the web version of this article.)

between the specimens and the liquid metal, knowledge of the flow field inside the test chamber is required. Furthermore, the extent of vertical flow is of interest for the oxygen transport inside the liquid metal. Therefore, the respective hydrodynamic equations were solved numerically using the simulation software COMSOL Multiphysics®.

3.1. Methodology

The simulation domain corresponds to the liquid metal filled part of the chamber, see Fig. 3. The default filling height is 120 mm, which means that the horizontal parts of the L-shaped baffles are fully submerged. Because the four baffles reduce the velocity in the upper part substantially, the deformation of the free liquid surface (liquid/gas interface) is not taken into account and the simulation domain is fixed. This is justified by a simulation with a filling height of 140 mm, showing a merely slight reduction of around 3% of the bulk velocity in the channel where the samples are located. A full-slip boundary conditions is applied at the free liquid surface, whereas a no-slip boundary condition is applied at all liquid/solid interfaces.

The z-axis of the coordinate system is chosen to coincide with the symmetry axis of the chamber and to have its origin at the base of the chamber (base of channel). A rotational motion $\vec{v} = \vec{\omega} \times \vec{r}$ with $\vec{\omega} = -\Omega\vec{e}_z$ is prescribed to all rotating parts, i.e., the shaft, the disk, the six connectors between disk and sample holders, the sample holders, and the specimens. Cylindrical samples with diameter 8 mm and length 20 mm as well as flat specimens with dimensions 27 × 8 × 2 mm are considered in the simulations. The cylindrical samples are positioned with their axes at $r = 172$ mm, whereas the inner surfaces of the flat samples are located 174 mm away from the z-axis.

To solve the hydrodynamic equations in the 3-dimensional (3D) simulation domain, incompressible flow is assumed, gravity is taken into account, and isothermal conditions are applied. The material properties of liquid Pb at 550 °C are used (Pb properties at 450 °C and 650 °C yield similar results, see below), which means that the kinematic viscosity is of the order of 10^{-7} m^2/s. For specimen velocities of order 1 m/s and typical specimen dimensions of 0.01 m, Reynolds numbers around 10^5 and thus the occurrence of turbulence are expected. Therefore, the Reynolds-averaged Navier-Stokes (RANS) k-ε model for turbulent flow is used with wall functions selected as wall treatment. Note that for a high-accuracy prediction of the flow field around specimens of different shapes and orientation, a turbulence model better suited for resolving the wake field and a more rigorous treatment of low Re numbers near

walls would be required. To maximize accuracy of the turbulence model selected for the present study, careful meshing aiming for a wall lift-off in viscous units, y^+, in the range 25–100 is done. The simulation domain is meshed using an unstructured tetrahedral mesh with corner refinement. Boundary layers are added at all solid walls, with four layers added at the walls of stationary components and six layers added at the walls of moving parts. Different meshes are used for the simulations to ensure mesh independence of the results. The final mesh consists of about 3×10^6 domain elements. All results of the 3D simulations presented below are fully developed, yet transient, converged solutions obtained by the so-called "frozen rotor" study. For a truly time-dependent solution, a transient study is required (the solution of the frozen-rotor study may serve as initial condition), which is exemplarily performed for a 2-dimensional (2D) simulation of the flow in the channel loaded with cylindrical specimens. The time-dependent study in 2D confirms that the bulk velocity of the liquid metal obtained in the frozen rotor study corresponds to the bulk velocity reached in the long-term limit of the transient study.

3.2. Numerical results

The angular velocity Ω set by the motor (100, 250, 400 rpm), the number of specimens (2, 6), and the specimen geometry (cylindrical, flat) were varied.

Fig. 4 shows the results of the 3D flow field simulation for a fully loaded chamber (6 pairs of sample holders and cylindrical specimens) exemplarily for an angular speed of 400 rpm. The qualitatively same flow patterns are observed for 250 rpm, though at a slower velocity scale, whereas minor deviations are obtained for 100 rpm. This indicates a fully turbulent flow at 250 and 400 rpm. The wall lift-off in viscous units, y^+, reaches the highest values at the outer stationary chamber wall, up to 110 for 100 rpm and up to 420 for 400 rpm. The corresponding wall lift-off in length units reaches 0.5 mm. The lower cut-off limit of y^+ (11.06) is in place for 100 rpm only, namely along the edge of the cylindrical elevation. In respective locations, the wall lift-off is around 0.1 mm, i.e., much smaller than the dimensions of the geometrical features.

As expected, the flow velocity is highest in the channel where the specimens move. This is seen in Fig. 4a (highest velocity magnitude of around 3 m/s appears red) and in Fig. 4b, where the most negative azimuthal velocity components of around −3 m/s appears dark blue. Generally lower speeds are obtained in the upper part of the liquid metal thanks to the action of the L-shaped baffles. Here, significant vertical and radial velocity components are achieved (Fig. 4b), indicating efficient mixing and oxygen transport. In the channel with the rotating specimens, the flow is mainly azimuthal, with an average bulk velocity between the specimens of around 0.75 m/s for 100 rpm, 1.9 m/s for 250 rpm, and 3.0 m/s for 400 rpm (Table 1). For Pb properties taken at 450 and 650 °C, respectively, the results are the same within the uncertainty range given. As demonstrated in Fig. 4c (plane 1), the distance between consecutive samples is large enough to avoid a pronounced influence of the preceding specimen on the flow pattern around each sample.

When the test chamber is loaded with only 2 cylindrical specimens instead of 6, the average bulk velocity in the channel is reduced, see Table 1, which means that the specimens achieve a higher velocity relative to the moving liquid metal. The relative speed between the specimens on their outer side and the liquid metal bulk velocity is also given in Table 1 for the different configurations simulated. Finally, a flat specimen geometry was implemented in the simulations. The deviation of the bulk velocity between cylindrical and flat specimens is

Table 1
Average bulk velocity (m/s) of liquid metal in channel of test chamber and relative speed (m/s) between the specimens' outer side and the liquid metal bulk velocity for different specimen loadings and rotational speeds. Bulk velocity given with an uncertainty of about ±10%, uncertainty of relative speed accordingly.

	Bulk velocity			Relative speed		
	100 rpm	250 rpm	400 rpm	100 rpm	250 rpm	400 rpm
6x cylindrical	0.75	1.9	3.0	1.1	2.7	4.4
2x cylindrical	0.55	1.4	2.2	1.3	3.2	5.2
6x flat	0.73	1.8	2.9	1.1	2.8	4.5

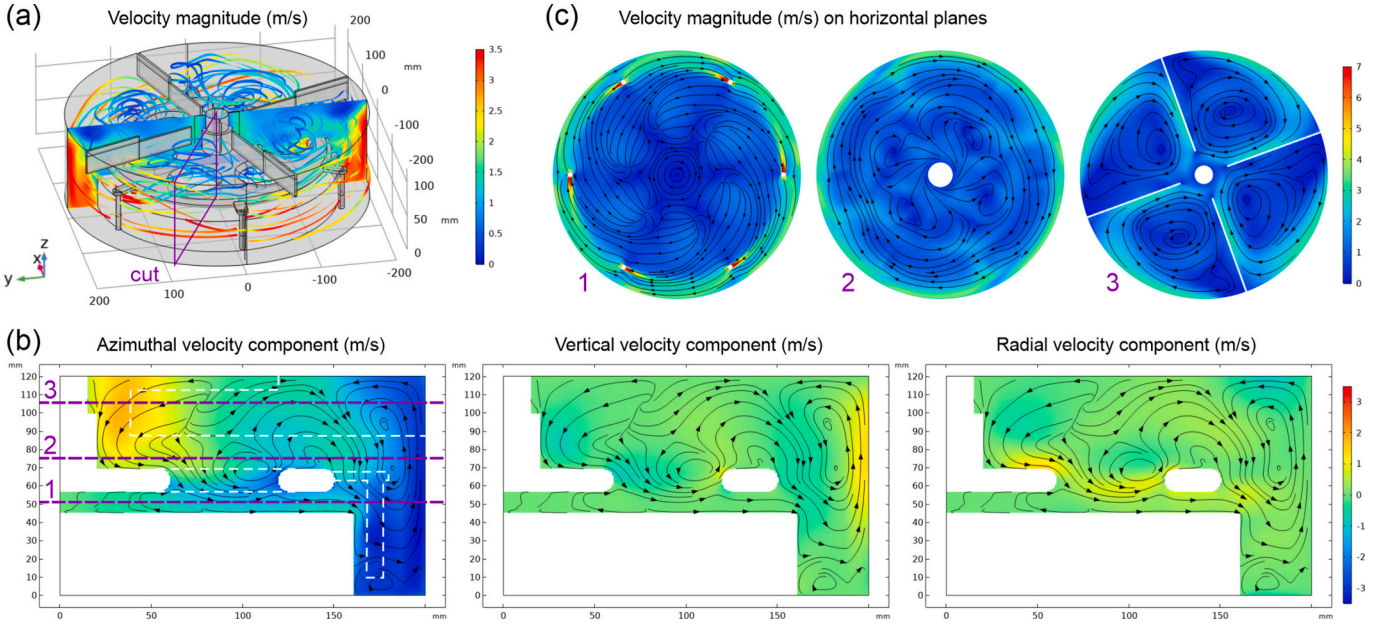

Fig. 4. Numerically solved 3D flow field for chamber loaded with 6 cylindrical samples at an angular speed of 400 rpm: (a) 3D view showing the velocity magnitude on the y-z plane and streamlines (color of streamlines also represents velocity magnitude), (b) results on vertical plane marked in (a) with the color representing the azimuthal (left image), vertical (middle), and radial (right image) velocity component, (c) results on horizontal planes as indicated in (b) with the color showing the velocity magnitude.

measurable but negligible, see Table 1 for respective numbers. However, flat samples are expected to experience higher shear rates around their edges compared with cylindrical samples.

4. Commissioning and first operation test

4.1. Materials and methods

For commissioning and the first functional check, the conditioning chamber was filled with pure Pb (purity 99.99%). Solid blocks were successively inserted and the chamber was heated until complete melting of a total of 12 L (136 kg) Pb was achieved. Since this process was done in atmosphere, Pb oxide formed on the surface of the molten Pb and the bulk of the liquid Pb became saturated in oxygen. Once all Pb was molten, the Pb oxide was removed from its surface and the conditioning chamber was closed. Using the gas control, further oxygen was removed from the liquid Pb until the desired exposure conditions were achieved (here: 450 °C and 10^{-7} wt% dissolved oxygen, obtained by using a gas mixture with a H_2/H_2O ratio of 0.2). The test chamber was loaded with four samples and hermetically closed. All specimens were made of stainless steel 316 L, two of them with flat rectangular geometry (named F1 and F2) and two with cylindrical shape (C1, C2). The dimensions were the same as in the simulations. The specimens were used as obtained from machining without any further surface treatment. The RMS surface roughness was 0.7 µm (F1, F2) and 0.9 µm (C1, C2), respectively.

Once the excess oxygen was removed from the molten Pb in the conditioning chamber and equilibrium was achieved, the Pb was transferred to the preheated test chamber, where it was again exposed to the gas control system and allowed time for equilibrating temperature and oxygen content. Unfortunately, because of insufficient preheating of the test chamber, the ceramic of the oxygen sensor in the test chamber broke upon contact with the hot Pb. Nevertheless, the test was started and the motor was set in motion. A rotational speed of 83 rpm was selected to achieve a relative velocity of 1.0 m/s between the samples and the liquid Pb. After 500 h of continuous motion at 450 °C, the motor was stopped, the liquid Pb was transferred back into the conditioning chamber, and the test chamber was allowed to cool down. Finally, the test chamber was opened and the samples were extracted. Adherent Pb was removed from the exposed samples by immersion into a 1:1:1 mixture of acetic acid, hydrogen peroxide, and ethanol for up to 30 min.

4.2. Experimental results

The photographs in Fig. 5 show the general appearance of the specimens after the 500-h erosion-corrosion test in liquid Pb at 450 °C. The surfaces got a blue-purple color where they were directly exposed to Pb, a typical sign for the growth of a thin oxide layer. The parts not in contact with Pb but with the sample holder (upper part of the inner surfaces of F1 and F2) show a brown color. There is one deviation from this general behavior. As visible in the photograph depicted in Fig. 5a, the outer surface of sample F1 shows a different color towards the rear end. Here, the blue color transitions via a bright stripe to a brown region.

On the surfaces with the typical blue-purple color, scanning electron microscopy (SEM, Zeiss LEO 1530 VP) images (signal from secondary electrons – SE) reveal that the coarse surface textures from machining are still there – no signs of dissolution corrosion or erosion-corrosion are observed (Fig. 6). Energy-dispersive X-ray analysis (EDX) also shows no indication of selective dissolution. However, in contrast to the surfaces prior to exposure (Fig. 6a), the coarse surface structures are decorated with fine crystals after exposure, presumably Fe-Cr-spinel. The presence of an oxide scale is confirmed by EDX, showing an oxygen enrichment at the surface, i.e., when the composition is measured with lower accelerating voltage. Although the exact oxygen content during the exposure is unknown due to the breakdown of the oxygen sensor in the test chamber, these results confirm the presence of oxygen dissolved in liquid Pb during the erosion-corrosion test in a concentration sufficient to grow an oxide scale and protect the steel from dissolution corrosion. This is a great achievement compared with the previous CORELLA and other rotating machines reported in literature, where only oxygen depleted conditions (~10^{-8} wt% and below) were realized (Choi et al., 2021; Martinelli et al., 2020; Wong et al., 2026; Heinzel et al., 2024). The absence of a thick layer of magnetite in the present commissioning test can have two reasons. Either the oxygen content was too low to support its growth or the fluid flow with 1 m/s relative speed prevented its growth to a continuous layer, i.e., magnetite formed but was instantly removed by the flow.

Finally, analysis of the region apparently affected by the liquid metal flow is presented, i.e., of the rear end of the outer surface of F1. Respective results obtained by a scanning profilometer (µscan from NanoFocus) and SEM are summarized in Fig. 7. The topography data obtained from the profilometer show that material is lost from the surface, with the flow-induced corrosion marks reaching a depth of 10–15 µm. SEM analysis confirms the loss of the machining-specific surface texture.

So far it remains unclear why only one of the two flat samples shows distinct signs of flow-induced corrosion while the other flat sample and the cylindrical samples do not show similar features. A possible explanation is that the sample F1 was unintentionally mounted with a slight angle relative to the flow direction, leading to an increased shear rate at the rear end of the outer surface. A respective improvement of the sample holders is planned to ensure a defined sample orientation. An alternative explanation of the more severe corrosion towards the rear end of F1 is a locally enhanced flow turbulence due to a sample irregularity. To critically test the hypothesis of an angular misalignment, further systematic erosion-corrosion tests at different angles and speeds are required, which are planned for future studies using the CORELLA-2 facility. The task of the commissioning test, however, was fulfilled. The CORELLA-2 was demonstrated to be an operational facility for erosion-corrosion tests under controlled temperature, oxygen content, and flow conditions, suitable for specimens of different shape. The facility's capabilities regarding higher temperature and speeds are to be

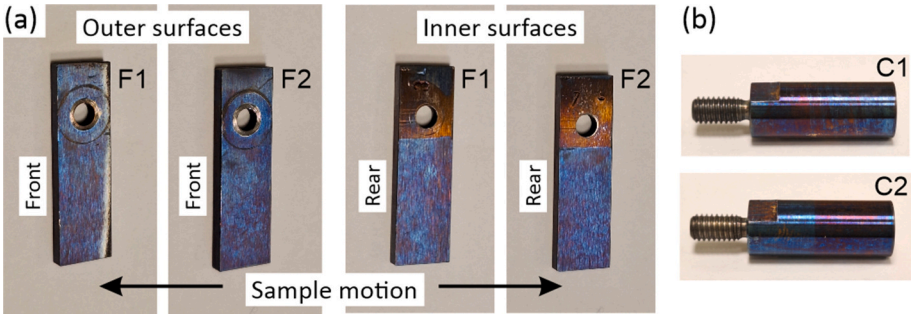

Fig. 5. Photographs of flat (a) and cylindrical (b) samples after erosion-corrosion test.

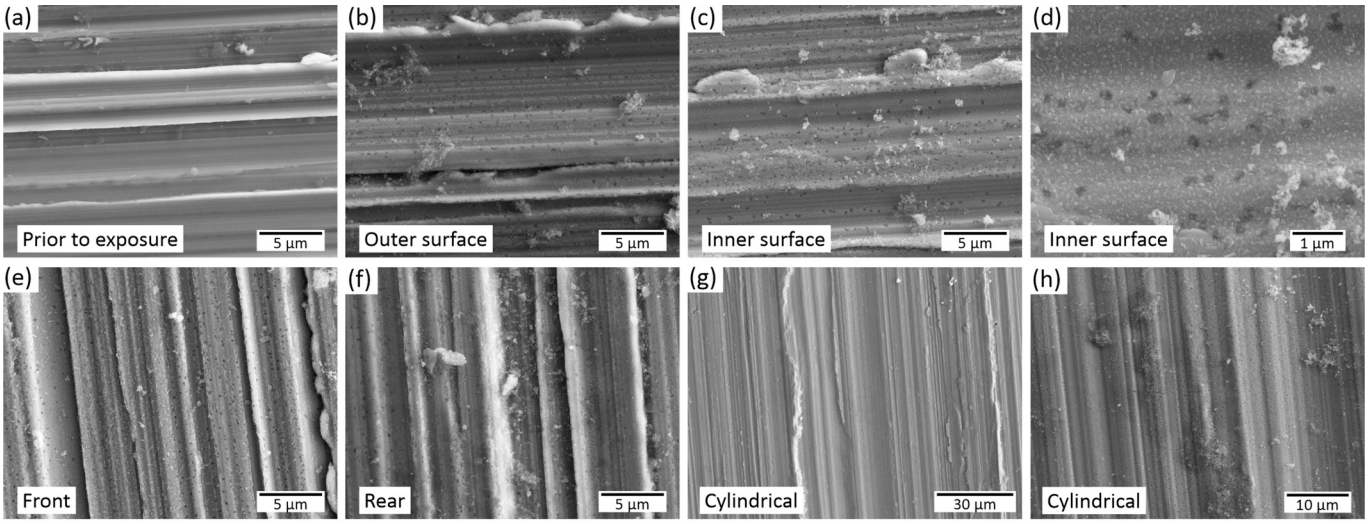

Fig. 6. Typical SEM-SE images of sample surfaces (a) prior to and (b)-(h) after erosion-corrosion test.

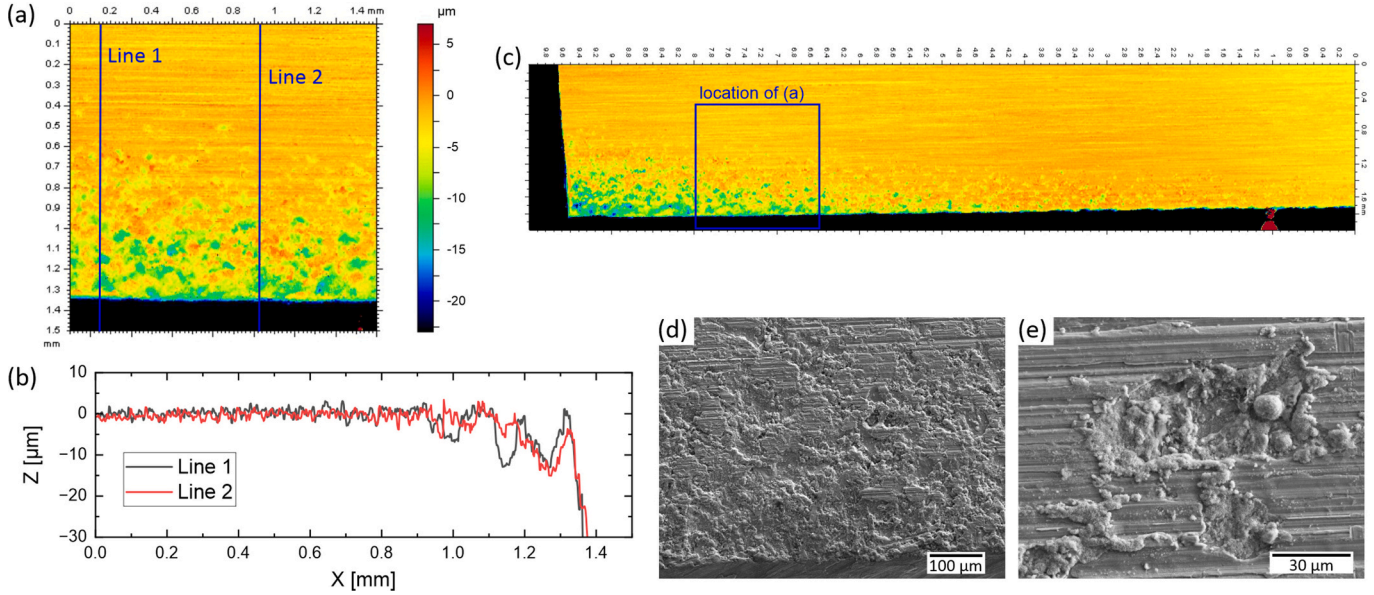

Fig. 7. Analysis of flow-affected corrosion region of sample F1. (a) High-resolution surface topography image, (b) line profiles extracted from (a), (c) overview topography image with same height scale as in (a), (d) low-magnification SEM-SE image, (e) SEM-SE image with higher magnification.

demonstrated in future tests.

5. Conclusion

This work introduced the new erosion-corrosion test facility CORELLA-2 for material testing in flowing Pb and Pb-alloys. The design and successful commissioning of CORELLA-2 was reported. CORELLA-2 enables exposures of up to six specimens at the same time, moving against the liquid metal under full control of temperature and oxygen concentration. Hereby, full flexibility of the sample shape and orientation is provided, only limited by the available space in the test chamber. CORELLA-2 is designed for temperatures up to 700 °C (operation at 450 °C has been experimentally demonstrated) and can operate at any desired oxygen concentration between depleted and saturated conditions. First experiments have demonstrated a successful run at a relative speed of 1 m/s between specimens and liquid Pb as determined by numerical simulations of the flow field during operation. Higher velocities and temperatures as well as systematic erosion-corrosion studies are planned for the near future.

CRediT authorship contribution statement

Renate Fetzer: Writing – original draft, Visualization, Methodology, Investigation. **Louis Müller:** Methodology, Investigation. **Fabian Lang:** Methodology, Investigation. **Annette Heinzel:** Methodology, Investigation, Writing – review & editing. **Alfons Weisenburger:** Writing – review & editing, Methodology. **Georg Müller:** Project administration.

Declaration of competing interest

The authors declare that they have no known competing financial interests or personal relationships that could have appeared to influence the work reported in this paper.

Acknowledgments

This project has received funding from the European Union Euratom Research and Training Programme under grant agreement No. 101166337 (LESTO project) and No. 101061241 (INNUMAT project). The content of this paper reflects only the authors' views and the European Commission cannot be held responsible for them.

Data availability

Data will be made available on request.

References

Alemberti, A., 2016. The lead fast reactor: an opportunity for the future? Engineering 2, 59–62. https://doi.org/10.1016/J.ENG.2016.01.022.

Ali, A.E.A., Cioncolini, A., Laurence, D., Iacovides, H., 2022. Liquid lead flow-accelerated corrosion testing with the rotating cage set-up: a CFD optimisation. Ann. Nucl. Energy 165, 108620. https://doi.org/10.1016/j.anucene.2021.108620.

Chakraborty, P., Kain, V., Pradhan, P.K., Fotedar, R.K., Krishnamurthy, N., Dey, G.K., 2015. Corrosion of Indian RAFMS in Pb–17Li in a rotating disc corrosion test facility at 773K. Fusion Eng. Design 100, 181–189. https://doi.org/10.1016/j.fusengdes.2015.05.053.

Chen, G., Ju, N., Lei, Y., Wang, D., Zhu, Q., Li, T., 2020. Corrosion behavior of base metal and weld bead of CLAM steel in flowing Pb-Bi at 550 °C. Prog. Nucl. Energy 118, 103074. https://doi.org/10.1016/j.pnucene.2019.103074.

Choi, J., Hwang, I., Lee, Y., 2021. Flow accelerated corrosion of stainless steel 316L by a rotating disk in lead-bismuth eutectic melt. JOM 73, 4030–4040. https://doi.org/10.1007/s11837-021-04953-y.

Cionea, C., Abad, M.D., Aussat, Y., Frazer, D., Gubser, A.J., Hosemann, P., 2016. Oxide scale formation on 316L and FeCrAl steels exposed to oxygen controlled static LBE at temperatures up to 800 °C. Sol. Energy Mater. Sol. Cells 144, 235–246. https://doi.org/10.1016/j.solmat.2015.09.007.

Dömstedt, P., Lundberg, M., Szakalos, P., 2019. Corrosion studies of low-alloyed FeCrAl steels in liquid lead at 750°C. Oxid. Met. 91, 511–524. https://doi.org/10.1007/s11085-019-09896-z.

Dömstedt, P., Lundberg, M., Szakálos, P., 2020. Corrosion studies of a low alloyed Fe–10Cr–4Al steel exposed in liquid Pb at very high temperatures. J. Nucl. Mater. 531, 152022. https://doi.org/10.1016/j.jnucmat.2020.152022.

Fazio, C., Ricapito, I., Scaddozzo, G., Benamati, G., 2003. Corrosion behaviour of steels and refractory metals and tensile features of steels exposed to flowing PbBi in the LECOR loop. J. Nucl. Mater. 318, 325–332. https://doi.org/10.1016/S0022-3115(03)00009-6.

Fetzer, R., Weisenburger, A., Mueller, G., 2021. Turbulent flow of liquid lead alloy in oxygen-controlled corrosion erosion test facility. AIP Adv. 11, 075303. https://doi.org/10.1063/5.0057380.

Handbook on Lead-bismuth Eutectic Alloy and Lead Properties, Materials Compatibility, Thermal-hydraulics and Technologies, 2015. OECD Publishing, Paris.

Heinzel, A., Hering, W., Konys, J., Marocco, L., Litfin, K., Müller, G., Pacio, J., Schroer, C., Stieglitz, R., Stoppel, L., Weisenburger, A., Wetzel, T., 2017. Liquid metals as efficient high-temperature heat-transport fluids. Energ. Technol. 5, 1026–1036. https://doi.org/10.1002/ente.201600721.

Heinzel, A., Fetzer, R., Lang, F., Weisenburger, A., Cataldo, S., Di Fonzo, F., Müller, G., 2024. Corrosion tests on austenitic samples with alumina and alumina-forming coatings in oxygen-containing stagnant Pb and turbulently flowing PbBi. J. Nucl. Mater. 596, 155121. https://doi.org/10.1016/j.jnucmat.2024.155121.

Jiang, H., Lu, W., Wang, W., Chen, Z., Chu, D., Han, J., Huang, Y., Wu, Y., 2020. Experimental study on corrosion-erosion behavior of ITER blanket structure materials in flowing Pb-17Li. Fusion Eng. Design 156, 111596. https://doi.org/10.1016/j.fusengdes.2020.111596.

Kieser, M., Muscher, H., Weisenburger, A., Heinzel, A., Müller, G., 2009. Liquid metal corrosion/erosion investigations of structure materials in lead cooled systems: part 1. J. Nucl. Mater. 392, 405–412. https://doi.org/10.1016/j.jnucmat.2008.12.327.

Kondo, M., Muroga, T., Sagara, A., Valentyn, T., Suzuki, A., Terai, T., Takahashi, M., Fujii, N., Yokoyama, Y., Miyamoto, H., Nakamura, E., 2011. Flow accelerated corrosion and erosion–corrosion of RAFM steel in liquid breeders. Fusion Eng. Des. 86, 2500–2503. https://doi.org/10.1016/j.fusengdes.2011.01.108.

Lambrinou, K., Charalampopoulou, E., Van der Donck, T., Delville, R., Schryvers, D., 2017. Dissolution corrosion of 316L austenitic stainless steels in contact with static liquid lead-bismuth eutectic (LBE) at 500°C. J. Nucl. Mater. 490, 9–27. https://doi.org/10.1016/j.jnucmat.2017.04.004.

Li, C., Liu, Y., Zhang, F., Fang, X., Liu, Z., 2021a. Erosion-corrosion of 304N austenitic steels in liquid PbBi flow perpendicular to steel surface. Mater Charact 175, 111054. https://doi.org/10.1016/j.matchar.2021.111054.

Li, C., Fang, X., Wang, Q., Shen, M., Wang, H., Zeng, X., Liu, Y., Meng, G., 2021b. A synergy of different corrosion failure modes pertaining to T91 steel impacted by extreme lead–bismuth eutectic flow pattern. Corros. Sci. 180, 109214. https://doi.org/10.1016/j.corsci.2020.109214.

Martinelli, L., Ginestar, K., Botton, V., Delisle, C., Balbaud-Célérier, F., 2020. Corrosion of T91 and pure iron in flowing and static Pb-Bi alloy between 450 °C and 540 °C: experiments, modelling and mechanism. Corros. Sci. 176, 108897. https://doi.org/10.1016/j.corsci.2020.108897.

Niedermeier, K., 2023. A perspective on high-temperature heat storage using liquid metal as heat transfer fluid. Energy Storage 5, e530. https://doi.org/10.1002/est2.530.

Pantaleo, A.M., Trevisan, S., Matteucci, F., Cabeza, L.F., 2024. Innovation trends on high-temperature thermal energy storage to defossilize energy systems. J. Energy Storage 103, 114261. https://doi.org/10.1016/j.est.2024.114261.

Popovic, M.P., Yang, Y., Bolind, A.M., Ozdol, V.B., Olmsted, D.L., Asta, M., Hosemann, P., 2018. Transmission electron microscopy (TEM) study of the oxide layers formed on Fe-12Cr-4Al ferritic alloy in an oxygenated Pb-Bi environment at 800 °C. JOM 70, 1471–1477. https://doi.org/10.1007/s11837-018-2951-8.

Popovic, M.P., Bolind, A.M., Aussat, Y., Gubser, A.J., Hosemann, P., 2019. Oxidative passivation of Fe–Cr–Al steels in lead-bismuth eutectic under oxygen-controlled static conditions at 700° and 800 °C. J. Nucl. Mater. 523, 172–181. https://doi.org/10.1016/j.jnucmat.2019.06.004.

Purwitasari, A., Oskay, C., Heinzel, A., Fetzer, R., Weisenburger, A., Müller, G., 2025a. Corrosion of austenitic stainless steels in liquid Pb with 2E-7 wt% oxygen at 600 and 700 °C. Corros. Sci. 244, 112651. https://doi.org/10.1016/j.corsci.2024.112651.

Purwitasari, A., Fetzer, R., Heinzel, A., Oskay, C., Weisenburger, A., Müller, G., 2025b. Pb corrosion of ferritic/martensitic steels at 600–700°C. Corros. Sci. 255, 113142. https://doi.org/10.1016/j.corsci.2025.113142.

Schroer, C., Wedemeyer, O., Novotny, J., Skrypnik, A., Konys, J., 2011. Long-term service of austenitic steel 1.4571 as a container material for flowing lead–bismuth eutectic. J. Nucl. Mater. 418, 8–15. https://doi.org/10.1016/j.jnucmat.2011.07.026.

Shi, H., Jianu, A., Weisenburger, A., Tang, C., Heinzel, A., Fetzer, R., Lang, F., Stieglitz, R., Müller, G., 2019. Corrosion resistance and microstructural stability of austenitic Fe–Cr–Al–Ni model alloys exposed to oxygen-containing molten lead. J. Nucl. Mater. 524, 177–190. https://doi.org/10.1016/j.jnucmat.2019.06.043.

Shi, H., Fetzer, R., Tang, C., Szabó, D.V., Schlabach, S., Heinzel, A., Weisenburger, A., Jianu, A., Müller, G., 2021. The influence of Y and Nb addition on the corrosion resistance of Fe-Cr-Al-Ni model alloys exposed to oxygen-containing molten Pb. Corros. Sci. 179, 109152. https://doi.org/10.1016/j.corsci.2020.109152.

Takaya, S., Furukawa, T., Müller, G., Heinzel, A., Jianu, A., Weisenburger, A., Aoto, K., Inoue, M., Okuda, T., Abe, F., Ohnuki, S., Fujisawa, T., Kimura, A., 2012. Al-containing ODS steels with improved corrosion resistance to liquid lead–bismuth. J. Nucl. Mater. 428, 125–130. https://doi.org/10.1016/j.jnucmat.2011.06.046.

Tsisar, V., Schroer, C., Wedemeyer, O., Skrypnik, A., Konys, J., 2014. Corrosion behavior of austenitic steels 1.4970, 316L and 1.4571 in flowing LBE at 450 and 550 °C with 10−7mass% dissolved oxygen. J. Nucl. Mater. 454, 332–342. https://doi.org/10.1016/j.jnucmat.2014.08.024.

Tsisar, V., Schroer, C., Wedemeyer, O., Skrypnik, A., Konys, J., 2016. Long-term corrosion of austenitic steels in flowing LBE at 400°C and 10−7 mass% dissolved oxygen in comparison with 450 and 550°C. J. Nucl. Mater. 468, 305–312. https://doi.org/10.1016/j.jnucmat.2015.09.027.

Vignarooban, K., Xu, X., Arvay, A., Hsu, K., Kannan, A.M., 2015. Heat transfer fluids for concentrating solar power systems – a review. Appl. Energy 146, 383–396. https://doi.org/10.1016/j.apenergy.2015.01.125.

Wallenius, J., 2019. Maximum efficiency nuclear waste transmutation. Ann. Nucl. Energy 125, 74–79. https://doi.org/10.1016/j.anucene.2018.10.034.

Wan, T., Saito, S., 2018. Flow-accelerated corrosion of type 316L stainless steel caused by turbulent lead–bismuth eutectic flow. Metals 8, 627. https://doi.org/10.3390/met8080627.

Wang, H., Qiu, X., Li, Y., Liu, B., Li, W., Su, D., Tang, Z., 2024. Short-term corrosion behavior and mechanism of 316 stainless steel in liquid Pb at 650 and 750°C. J. Mater. Eng. Perform. 33, 7210–7221. https://doi.org/10.1007/s11665-023-08479-z.

Wang, R., Qiu, X., Gao, S., Liu, W., Li, W., Li, Y., Tang, Z., 2022. Corrosion behavior of 316 stainless steel arc parts in liquid lead at 650°C under high oxygen concentrations. RSC Adv. 12, 32700–32707. https://doi.org/10.1039/D2RA05165F.

Weisenburger, A., Heinzel, A., Müller, G., Muscher, H., Rousanov, A., 2008. T91 cladding tubes with and without modified FeCrAlY coatings exposed in LBE at different flow, stress and temperature conditions. J. Nucl. Mater. 376, 274–281. https://doi.org/10.1016/j.jnucmat.2008.02.026.

Wong, K.W., Mickus, I., Torkelson, N., Vasudevan, S., Li, H., Grishchenko, D., Kudinov, P., 2024. Hydrodynamic design of the Separate Effect test facility for Flow-Accelerated Corrosion and Erosion (SEFACE) studies in liquid lead. Nucl. Eng. Des. 417, 112852. https://doi.org/10.1016/j.nucengdes.2023.112852.

Wong, K.W., Szakálos, P., Petersson, C., Grishchenko, D., Kudinov, P., 2026. Mechanistic insight into the ferritization of austenite in Pb via a discontinuous reaction governed by a migrating liquid film. Corros. Sci. 258, 113398. https://doi.org/10.1016/j.corsci.2025.113398.

Zhang, J., 2009. A review of steel corrosion by liquid lead and lead–bismuth. Corros. Sci. 51, 1207–1227. https://doi.org/10.1016/j.corsci.2009.03.013.